# Designing efficient spin Seebeck-based thermoelectric devices via simultaneous optimization of bulk and interface properties

## Electronic Supplementary Information

Min Young Kim,[a] Sang J. Park,[a] Gi-Yeop Kim,[b,c] Si-Young Choi[b,c] and Hyungyu Jin[a,*]

[a]*Department of Mechanical Engineering, Pohang University of Science and Technology (POSTECH), Pohang 37673, South Korea. E-mail: hgjin@postech.ac.kr*

[b]*Department of Materials Science and Engineering, Pohang University of Science and Technology (POSTECH), Pohang 37673, South Korea.*

[c]*Materials Imaging & Analysis Center, Pohang University of Science and Technology (POSTECH), Pohang 37673, South Korea.*

[*] Correspondence should be addressed to H. J.

## I. Two-step sintering temperature process

Three different temperature profiles (**Fig. S1**) were used to sinter the cold-pressed $NiFe_2O_4$ (NFO) pellets. Particularly, the two-step sintering process was used for each sample to obtain fully dense samples. For NFO1623, the first sintering temperature and sintering time were 1473 K and 7 h; then, the second temperature and time changed to 1623 K and 10 h. For NFO1673 and NFO1723, they were sintered at 1473 K for 20 h first, and then maintained at 1673 K and 1723 K for 20 h, respectively. A heating rate remained constant at ~5 $K \cdot min^{-1}$ to prevent the samples from being thermally damaged. After each sintering process, the samples were cooled down to 1073 K at 5 $K \cdot min^{-1}$. Then, slow natural cooling was followed until room temperature. During the sintering process, the monoxide phase was formed from the NFO spinel phase by referring to the Ni-Fe-$O_2$ phase diagram[1] (**Fig. S2**).

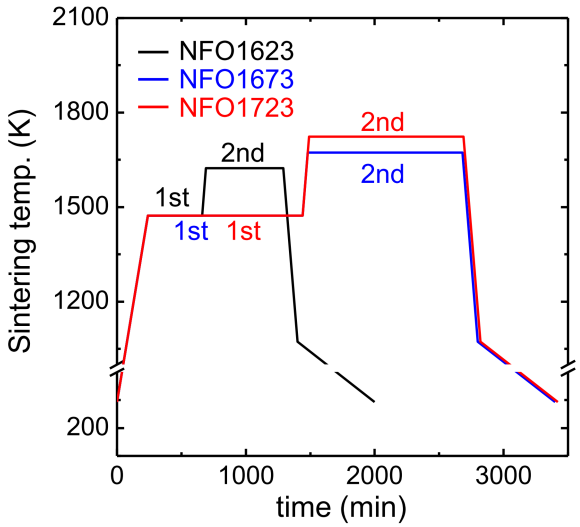


**Fig. S1** Three different two-step sintering temperature profiles for NFO1623, NFO1673, and NFO1723.

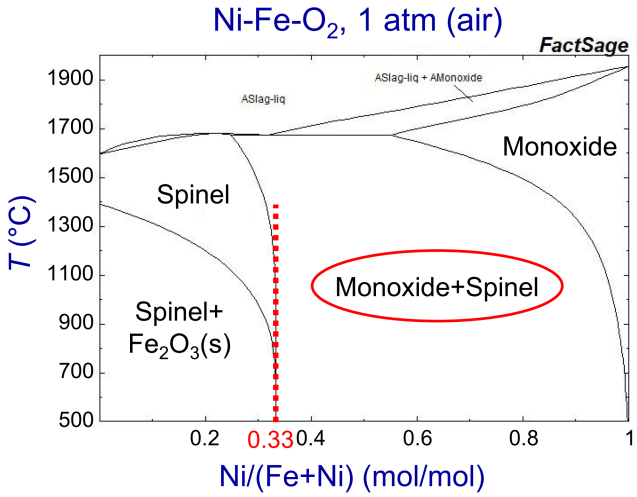


**Fig. S2** Ni-Fe-$O_2$ phase diagram with $p(O_2)$ = 0.21 atm reproduced from ref. [1] ($T$: temperature).

## II. Crystal structure analysis using powder X-ray diffraction

Crystal structure of the NFO samples were analyzed by powder X-ray diffraction (PXRD) for $2\theta$ from 20° to 70° (D/Max-2500, Rigaku). Phase constitutions and lattice parameters of the NFO matrix were estimated using the JADE software. All PXRD peaks agrees with standard PDF values (CDS, 86-2267) of NFO material (**Fig. S3**). These results indicate that the NFO phase was well formed during the sintering. The lattice parameter of each sample remained constant (~8.335 Å) regardless of the increase in sintering temperature.

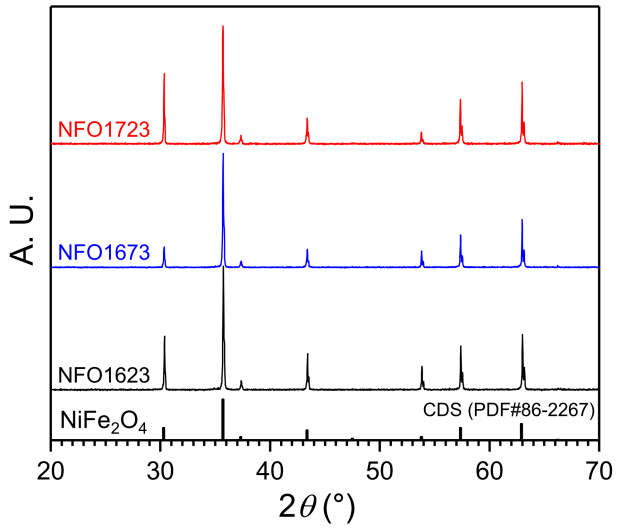


**Fig. S3** Powder X-ray Diffraction (PXRD) patterns of NFO1623, NFO1673, and NFO1723 after the sintering process.

## III. Spin Seebeck voltage measurements

Spin Seebeck coefficient $\alpha_{SSE}$ is defined as $\alpha_{SSE} = E_{ISHE} / \nabla T_z = \frac{\Delta V_{ISHE} / 2L_y}{\Delta T_z / L_z}$, where $E_{ISHE}$ is an electrical field induced by the ISHE in $y$-direction, $\Delta V_{ISHE}$ is a difference between saturation voltages in the $V_{ISHE}$ vs. $H$ curves (**Fig. S4b**), $L_y$ is distance between two electrodes on Pt, $\nabla T_z$ ($\Delta T_z$) is a temperature gradient (difference) on the sample in $z$-direction, and $L_z$ is thickness of NFO/Pt samples.

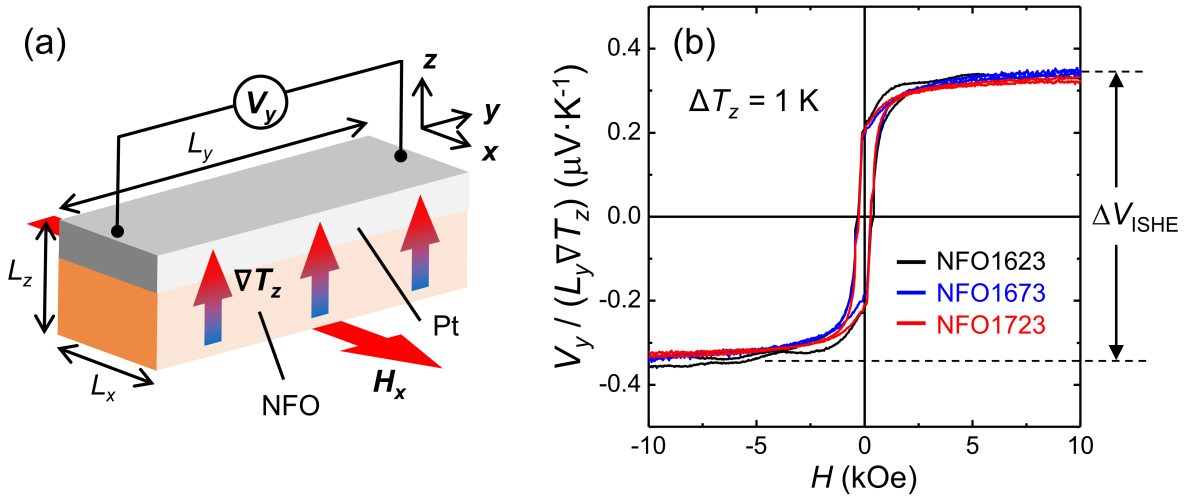


**Fig. S4** (a) An experimental configuration for spin Seebeck voltage measurements in a liquid-nitrogen cryostat system. (b) Magnetic field $H$ dependence of normalized spin Seebeck voltage $V_y / (L_y \nabla T_z)$ at 300 K for the NFO/Pt samples. ($V_y$ : measured spin Seebeck voltage, $L_y$ : distance between the two electrodes on Pt, $\nabla T_z$ ($\Delta T_z$): temperature gradient (difference) in the $z$-direction, $\Delta V_{ISHE}$ : difference between two saturation voltages in $V_y$ and $L_z$ : thickness of NFO/Pt samples)

## IV. Microstructures observation using scanning electron microscopy

The Fe-doped NiO precipitate is surrounded by the NFO matrix (**Fig. S5**) and its size increases with the sintering temperature. Here, we averaged 20 measured values of the size for each sample to obtain statistically meaningful results. The measured size increases from 4.2 μm to 9.5 μm as described in the main text.

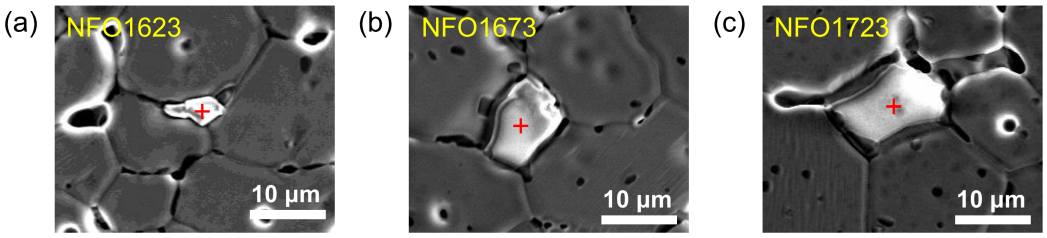


**Fig. S5** FE-SEM images of Fe-doped NiO precipitate in NFO matrix of (a) NFO1623, (b) NFO1673, and (c) NFO1723.

## V. Mass magnetization measurements using vibrating sample magnetometer

Mass magnetization were measured by a vibration sample magnetometer (VSM) (Quantum Design, Inc.). Magnetic field $H$ was swept at ~100 Oe·s$^{-1}$ in the range of $|H| < 10$ kOe at room temperature. Saturation magnetization $M_s$ of the NFO samples decreases with the sintering temperature, and reaches the minimum of 47.2 emu·g$^{-1}$ for NFO1723 (**Fig. S6**). The decrease in $M_s$ may result from transformation of a small amount of Ni and Fe ions into very weak ferromagnetic Fe-doped NiO.[2]

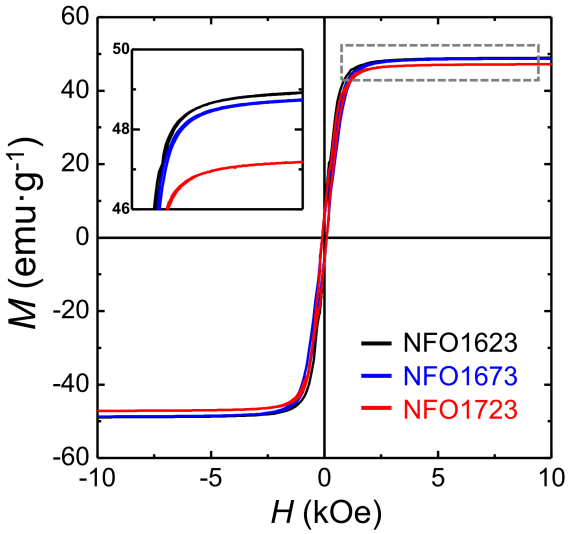


**Fig. S6** Magnetic field $H$ dependence of mass magnetization $M$ of NFO1623, NFO1673 and NFO 1723. (inset) Magnification of grey dashed region.

## VI. Structure, composition, morphology and strain analysis using scanning transmission electron microcopy

The scanning transmission electron microcopy (STEM) imaging was used to analyze the morphology and chemical composition of the Fe-doped NiO precipitate of NFO1723. First, the STEM specimen of NFO1723 was prepared by the focused ion beam system. The Fe-doped NiO precipitate (**Fig. S7a**) was deeply embedded in the NFO matrix (**Fig. S7b**). The chemical composition near and inside the Fe-doped NiO precipitate was examined by the STEM-EDS (**Table S1**); Eight red spots were detected (**Fig. S7c** and **Fig. S7d**). The spot 3, 4 and 5 have the chemical composition of Fe-doped NiO, and the near-surface spot 4 have higher oxygen atomic content than the embedded spot 3 because of exposure to air. However, the spot 1, 2, 7 and 8 have similar atomic ratios of ~1:3:6, which agrees well with Ni-deficient $Ni_{1-\delta}Fe_2O_4$. The spot 6 has Ni-richer composition than the spot 7 and 8 because the Fe-doped NiO and NFO phases may be mixed with different ratios by each spot due to their diverse growth rates.

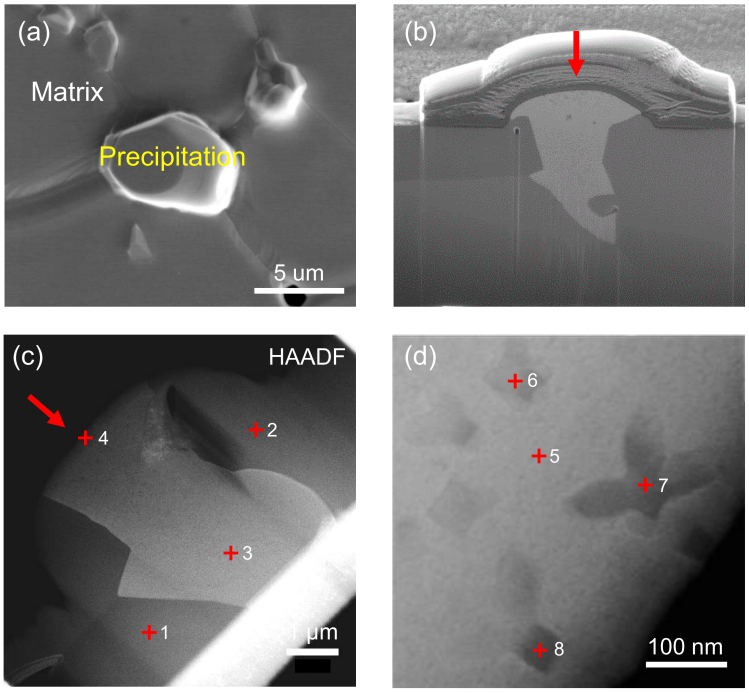


**Fig. S7** STEM images of the Fe-doped NiO precipitate of NFO1723 from (a) top view and (b) cross-section view. The observation spots for STEM-EDS (c) near and (d) inside the Fe-doped NiO precipitate.

| Spectrum number | Element content (at.%) | | |
|---|---|---|---|
| | Ni | Fe | O |
| 1 | 11.96 | 28.87 | 59.18 |
| 2 | 10.77 | 27.10 | 62.13 |
| 3 | 44.32 | 5.48 | 50.20 |
| 4 | 39.41 | 3.21 | 57.38 |
| 5 | 47.07 | 7.56 | 45.37 |
| 6 | 19.92 | 26.93 | 53.14 |
| 7 | 9.80 | 30.21 | 59.99 |
| 8 | 10.65 | 31.63 | 57.72 |

**Table S1** Chemical composition near and inside the NiO precipitate of NFO1723.

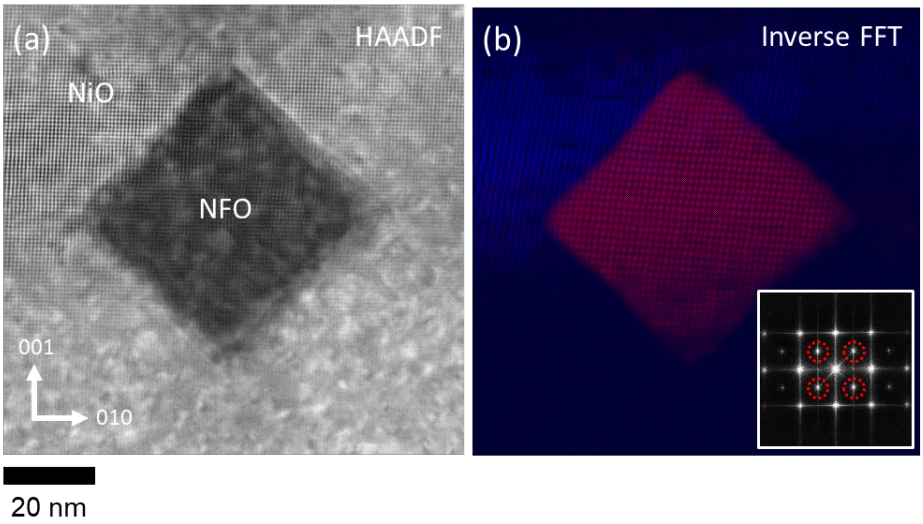


**Fig. S8** (a) A HAADF-STEM image of nano-NFO precipitate surrounded by micro-NiO precipitate and (b) an inverse FFT image of the HAADF-STEM image along [100] axis. Inverse FFT image was acquired by masking reflection (red-dot circles) in (inset).

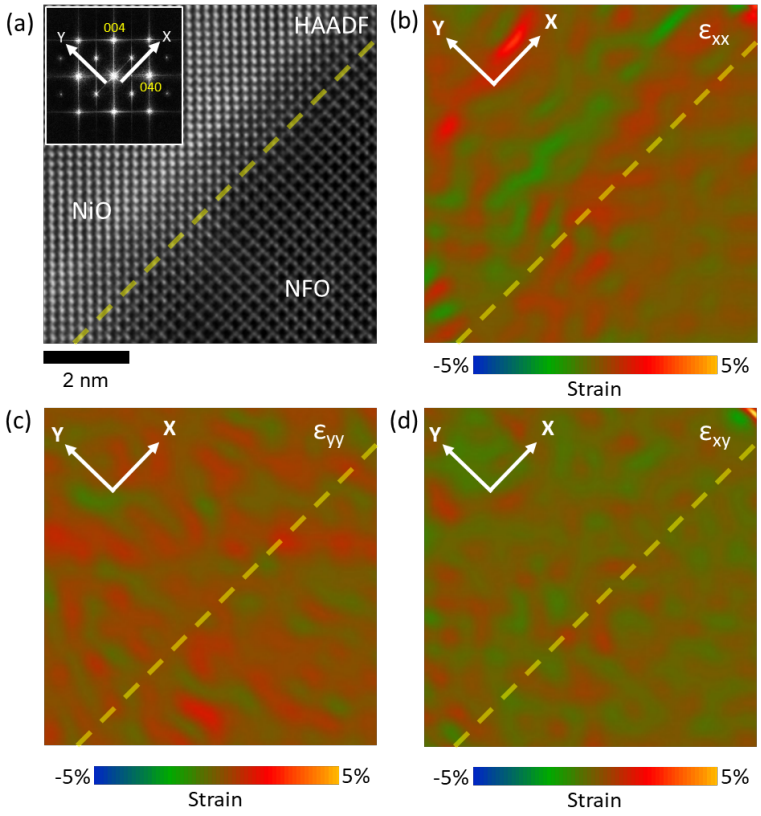


**Fig. S9** Strain mapping using geometrical phase analysis (GPA) between micro-NiO and nano-NFO precipitate. (a) A High resolution HAADF-STEM image for the strain mapping. Fourier vectors $x$ = [044] and $y$ = [0-44]. (b)-(d) Strain $\varepsilon_{xx}$, $\varepsilon_{yy}$ and $\varepsilon_{xy}$ maps from the FFT patterns. Yellow dash lines mark interface between micro-NiO/nano-NFO at all images.

## VII. A curve fitting analysis for a measured thermal conductivity

The curve fitting analysis was used to quantitatively estimate the Umklapp, nano-precipitates and boundary contributions to the lattice thermal conductivity $\kappa_L$ of our samples. First, Eq. (2) in the main text can be rewritten as

$$\kappa_L = \frac{1}{2\pi^2 v_g}\frac{k_B{}^4 T_D{}^3}{\hbar^3}\left(\frac{1}{x}\right)^3 \int_0^x \tau_{tot}\frac{t^4 e^t}{(e^t-1)^2}dt \text{ , (S1)}$$

where $x = T_D/T$ ($T_D$: Debye temperature) and $v_g$ is assumed to be constant by the Debye theory.[3] The integral term $I$ of Eq. (S1) can be simplified to

$$I = \frac{1}{A}\int_0^x \frac{t^4 e^t}{(t^2 + B/A)(e^t-1)^2}dt \cong \frac{1}{A}\int_0^x \frac{at^2}{t^2+B/A}dt = \frac{a}{A}\left(x - \sqrt{\frac{B}{A}}\tan^{-1}\left(\frac{x}{\sqrt{B/A}}\right)\right), \text{ (S2)}$$

where $a = 0.8814$, $A = \varphi\omega_D{}^2 x^{-3} e^{-x/3}$ and $B = \tau_{np}{}^{-1} + \tau_u{}^{-1}$ combined with Eq. (3) and (4) in the main text. Here, $\omega_D$ is the Debye phonon frequency estimated from the published $T_D$ = 441 K[4] of NFO material. Then, $\kappa_L$ can be expressed as

$$\kappa_L = \frac{aC}{\varphi}\left(xe^{x/3} - \sqrt{\frac{B}{\varphi\omega_D{}^2}}x\sqrt{x}e^{x/2}\tan^{-1}\left(\sqrt{\frac{\varphi\omega_D{}^2}{B}}\frac{e^{-x/6}}{\sqrt{x}}\right)\right), \text{ (S3)}$$

where $C = \frac{k_B{}^2}{2\pi^2\hbar}\frac{T_D}{v_g}$. So, $\varphi$ and each scattering rate of $\tau_u{}^{-1}$ and $\tau_{np}{}^{-1}$ at 300 K can be estimated (**Table 1** in the main text) by the curve fitting analysis with the conventional law $\tau_b{}^{-1} = v_g / L$ ($L$: grain size). When $\tau_u{}^{-1}$ is defined with average phonon frequency

$$\omega_{avg} = \frac{\int_0^{\omega_D}\omega D(\omega)d\omega}{\int_0^{\omega_D} D(\omega)d\omega} \text{ (S4)}$$

of NFO material with the density-of-states $D$ of lattice, the estimates of $\varphi$ and $\tau_u{}^{-1}$ are almost constant regardless of the change in the sintering temperature, and the fitted $\varphi$ agrees well with the calculated $\varphi = 9.19\cdot10^{-17}$ s as described in the main text. In contrast, $\tau_{np}{}^{-1}$ gradually increases with the sintering temperature; this result indicates that the nano-precipirates scattering strongly decreases $\kappa_L$ as confirmed in the measured $\kappa_{NFO}$. However, $\tau_b{}^{-1}$ has one order of magnitude lower than the other scattering rates; therefore, it is expected to hardly affect $\kappa_L$.

## VIII. Grain size measurements using electron back scattered diffraction

The grain size of the samples increases with the sintering temperature and reaches the maximum of 23.0 μm for NFO1723. The considerable grain growth may be contributed to efficient heat diffusion in NFO precursor powder with the high sintering temperature and long sintering time. Here, we averaged five measured values of the grain size for each sample to obtain statistically meaningful results and specified standard deviations (**Fig. S10d**–**S10f**).

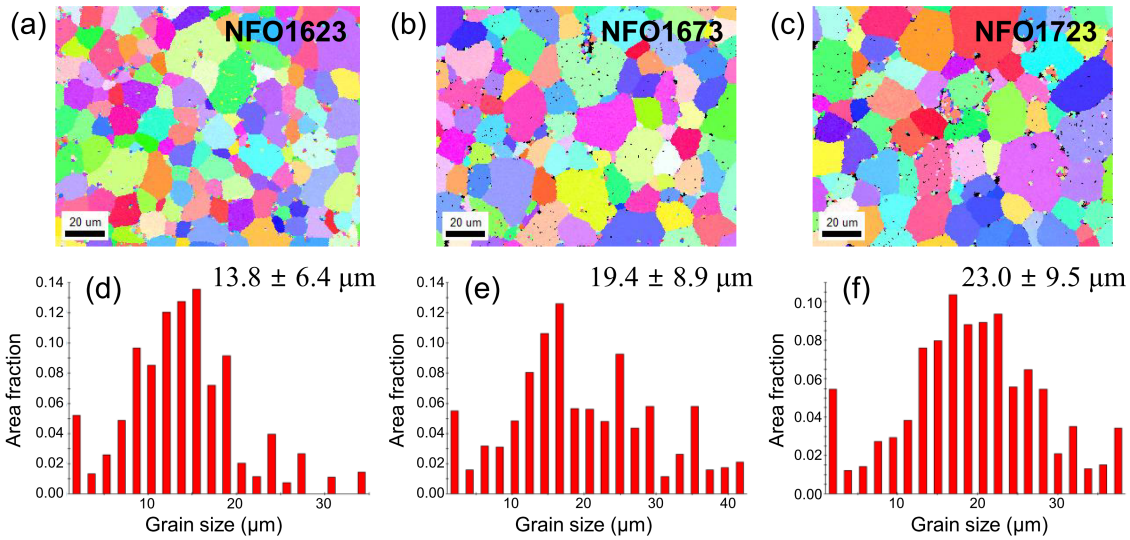


**Fig. S10** EBSD inverse pole figure maps and corresponding grain size distributions of NFO 1623 ((a) and (d)), NFO1673 ((b) and (e)), and NFO1723 ((c) and (f)).

## IX. Spin pumping efficiency estimation

Qualitative spin pumping efficiency $\xi$ can be estimated by using the relation between $j_s^0 / \nabla T_z$ and surface morphological characteristics of NFO samples in our previous work.[5] In this work, the SSE measurements were performed on seven NFO samples with different surface morphology each other; therefore, differences of $j_s^0 / \nabla T_z$ among the samples were attributed to only $\xi$.

The $j_s^0 / \nabla T_z$ of previous NFO samples has a linear dependence on active area fraction (**Fig. S11a**) whereas has no noticeable change by surface roughness (**Fig. S11b**); that is, $j_s^0 / \nabla T_z$ relies on only the active area fraction. So, we will exploit this result to predict $\xi$ of each as follows. Since the seven NFO/Pt samples have the same magnon accumulation $\left( j_s^0 / \nabla T_z \right) / \xi$ in the bulk NFO, we can infer normalized spin pumping efficiency $\xi_{\text{norm}}$ for each sample as

$$\xi_{\text{norm}} = \xi / \xi_0 = \left( j_s^0 / \nabla T_z \right) / \left( j_s^0 / \nabla T_z \right)_0 . \quad \text{(S5)}$$

where $\xi_0$ and $\left( j_s^0 / \nabla T_z \right)_0$ is the spin pumping efficiency and the pumped magnon current density of sample having the lowest $j_s^0 / \nabla T_z$ (red circle mark in **Fig. S11a**). In Eq. (S5), $\xi$ is proportional to $\xi_{\text{norm}}$; thus, the spin pumping efficiency of each sample can be easily compared using $\xi_{\text{norm}}$ itself instead of $\xi$. As shown in **Fig. S11c**, $\xi_{\text{norm}}$ from the previous work increases with the active area fraction similarly with $j_s^0 / \nabla T_z$ in **Fig. S11a**. So, we can estimate $\xi_{\text{norm}}$ of present samples by the least square fitting because the values of their active area fraction are known as described in the main text (**Fig. S11c**).

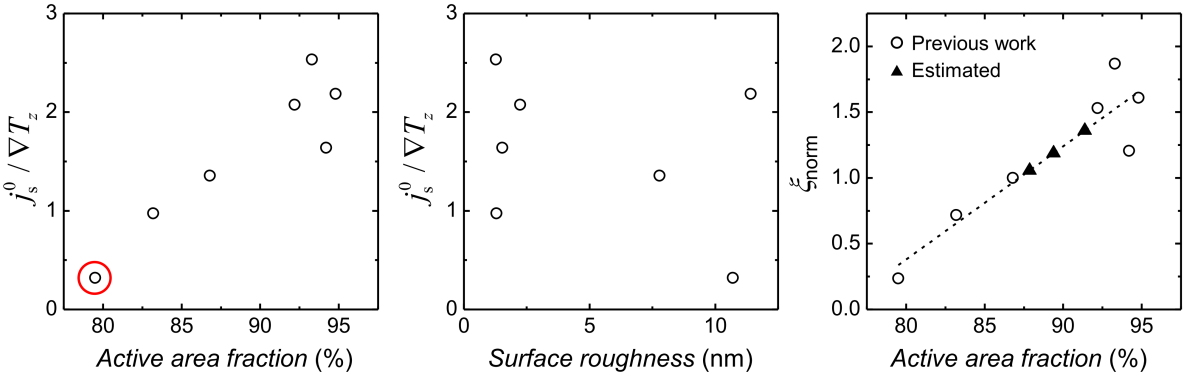


**Fig. S11** (a) Spin current density $j_s^0 / \nabla T_z$ versus active area fraction and (b) $j_s^0 / \nabla T_z$ versus surface roughness fraction of previous NFO samples. (c) Normalized spin pumping efficiency $\xi_{\text{norm}}$ versus active area fraction of previous (empty circles) and current (full triangles) NFO samples.

## X. Critical exponents for bulk magnon contribution

The critical exponent $\eta$ for the bulk magnon contribution to SSE is estimated by fitting the experimental data of temperature dependence of $(j_s^0/\nabla T_z)/\xi_{norm}$ (**Fig. S12**) with the following equation:[6, 7]

$$(j_s^0/\nabla T_z)/\xi_{norm} = S(T_c - T)^{\eta}, \quad \text{(S6)}$$

where both $S$ and $\gamma$ are adjustable parameters and $T_c$ is the Curie temperature of bulk NFO material.[8] The exponents are almost the same for all samples: 1.4 for NFO1623, 1.6 for NFO1673 and 1.6 for NFO1723. Those results support that the magnon propagation in bulk NFO is hardly affected by the presence of nano-precipitates or grain boundaries.

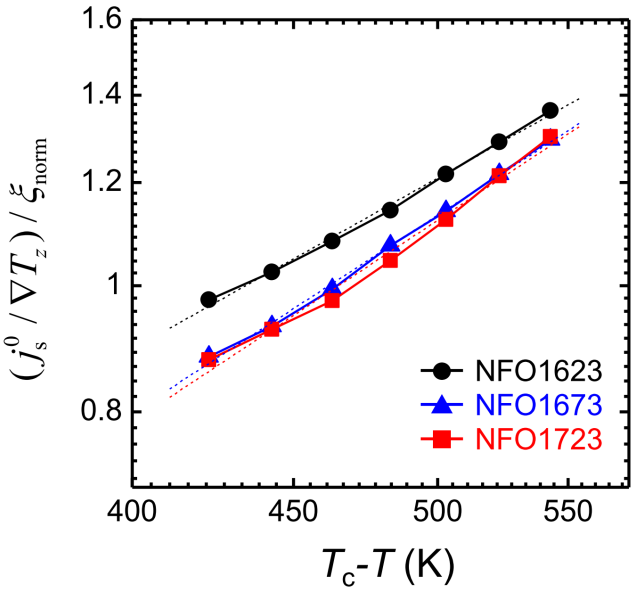


**Fig. S12** (a) The normalized bulk magnon current density $(j_s^0/\nabla T_z)/\xi_{norm}$ versus $T_c$ - $T$ ($T_c$: Curie temperature of NFO material and $T$: sample temperature).

## References


1. The phase diagram of Fe-Ni-$O_2$ in air, https://www.crct.polymtl.ca/fact/phase_diagram.php?file=Fe-Ni-O_Fe-Ni-O2_air.jpg&dir=FToxid, (accessed February, 2021).
2. R. Krishnakanth, G. Jayakumar, A. Albert Irudayaraj and A. Dhayal Raj, *Mater. Today: Proc.*, 2016, **3**, 1370-1377.
3. N. W. Ashcroft and N. D. Mermin, *Solid State Physics*, Cengage Learning, Belmont, 1976.
4. P. Chavan, L. R. Naik, P. B. Belavi, G. Chavan, C. K. Ramesha and R. K. Kotnala, *J. Electron. Mater.*, 2017, **46**, 188-198.
5. M. Kim, S. J. Park and H. Jin, *J. Appl. Phys.*, 2020, **127**, 085105.
6. K. Uchida, T. Kikkawa, A. Miura, J. Shiomi and E. Saitoh, *Phys. Rev. X*, 2014, **4**, 041023.
7. A. Miura, T. Kikkawa, R. Iguchi, K. Uchida, E. Saitoh and J. Shiomi, *Phys. Rev. Mater.*, 2017, **1**, 014601.
8. G. Nabiyouni, M. J. Fesharaki, M. Mozafari and J. Amighian, *Chin. Phys. Lett.*, 2010, **27**, 126401.